

Fusing numerical relativity and deep learning to detect higher-order multipole waveforms from eccentric binary black hole mergers

Adam Rebei,^{1,2} E. A. Huerta,^{1,3} Sibo Wang,^{1,3,4} Sarah Habib,^{1,5}
Roland Haas,¹ Daniel Johnson,^{1,4,5,6} and Daniel George^{1,3}

¹*NCSA, University of Illinois at Urbana-Champaign, Urbana, Illinois 61801, USA*

²*The University of Illinois Laboratory High School, University of Illinois at Urbana-Champaign, Urbana, Illinois 61801, USA*

³*Department of Astronomy, University of Illinois at Urbana-Champaign, Urbana, Illinois 61801, USA*

⁴*Department of Computer Science, University of Illinois at Urbana-Champaign, Urbana, Illinois, 61801*

⁵*Department of Physics, University of Illinois at Urbana-Champaign, Urbana, Illinois 61801, USA*

⁶*Students Pushing INnovation (SPIN) undergraduate intern at NCSA*

(Dated: November 19, 2019)

An ever increasing number of gravitational wave detections with the LIGO and Virgo observatories has firmly established the existence of binary black hole mergers. Elucidating the astrophysical environments where these objects form and coalesce is an active area of research. Motivated by recent electromagnetic observations which suggest the existence of compact binary populations in the Galactic Cluster M22 [1] and in the Galactic center [2], and considering that eccentricity provides one of the cleanest signatures to identify these compact binary populations, in this article we study the importance of including higher-order waveform multipoles to enable gravitational wave observations of eccentric binary black hole mergers. Using a catalog of **Einstein Toolkit** numerical relativity simulations that describe eccentric, non-spinning black holes mergers with mass-ratios $1 \leq q \leq 10$, and eccentricities $e_0 \lesssim 0.2$ ten cycles before merger, we determine the mass-ratio, eccentricity and binary inclination angle combinations that maximize the contribution of the higher-order waveform multipoles $(\ell, |m|) = \{(2, 2), (2, 1), (3, 3), (3, 2), (3, 1), (4, 4), (4, 3), (4, 2), (4, 1)\}$ for gravitational wave detection. We then explore the implications of these results in the context of stellar mass black holes that are detectable by LIGO detectors at design sensitivity, and show that compared to models that only include the $(\ell, |m|) = (2, 2)$ mode, the inclusion of higher-order waveform multipoles can increase the signal-to-noise ratio of eccentric binary black hole mergers by up to $\sim 45\%$ for mass-ratio binaries $q \leq 10$. Furthermore, building upon our pioneering deep learning work [3, 4], we show for the first time that machine learning can accurately reconstruct higher-order waveform multipole signals from eccentric binary black mergers embedded in real LIGO data.

I. INTRODUCTION

The LIGO [5, 6] and Virgo [7] gravitational wave (GW) detectors have enabled the detection of several GW sources that are consistent with the astrophysical properties of binary black hole (BBH) mergers [8–12] and neutron star collisions [13]. These scientific discoveries have firmly established GW astrophysics, and initiated the era of multi-messenger astrophysics (MMA) [13–15].

With an ever increasing catalog of GW sources, it will be possible to carry out robust statistical analyses to infer astrophysical properties of compact binary populations. Of special interest in this article is the study of compact binary populations in dense stellar environments. The observation of stellar mass BHs in the Galactic cluster M22 [1] triggered the improvement of algorithms to numerically simulate the formation, retention and detection of BBHs in dense stellar environments [16–19]. Using adequate simulation tools, it has been recently shown that the detection rate of these events has been significantly underestimated in previous analyses [20–25]. At the same time, using state-of-the-art waveform models that describe the inspiral-merger-ringdown of eccentric BBH mergers, it has been shown that the existing catalog of detected BBH mergers may have eccentricity content

at lower frequencies, $e \lesssim 0.1$ at 10Hz, and still be consistent with quasi-circular BBH mergers in the frequency band in which they were observed by the LIGO and Virgo detectors [26, 27]. This is because GWs are very effective at circularizing compact binary systems [26, 28–31]. Another line of evidence for the existence of eccentric compact binary mergers is the recent observation of compact remnants in the Galactic center, consistent with the prediction of a population of stellar mass BHs near supermassive BHs in galactic nuclei [2].

While the existence of eccentric compact binary mergers is well motivated, the most sensitive tools that have been developed for GW discovery are tailored for the identification of quasi-circular binaries [32, 33]. In order to accelerate these detection algorithms, and enable the identification of new classes of GW sources, such as eccentric compact binary mergers, authors in this manuscript pioneered the use of deep learning for GW data analysis [3, 4]. These algorithms have been proven to successfully identify, reconstruct and denoise eccentric numerical relativity (NR) waveforms that contain the dominant $(\ell, |m|) = (2, 2)$ mode embedded both in simulated and real LIGO data [3, 4, 34]. In view of these developments, and realizing that the vast majority of eccentric waveform models have only used the dominant $(\ell, |m|) = (2, 2)$

mode [26, 27, 35–46], in this work we quantify the importance of including higher-order waveform multipoles for the detection of eccentric BBH mergers, and also show that our deep learning algorithms can accurately identify higher-order waveform multipole signals in simulated and real LIGO data. This is the first analysis of this nature in the literature in the context of eccentric BBH mergers.

Throughout this article, we use natural units $G = c = 1$, and denote the masses of the binary components by $m_{\{1,2\}}$ ($m_1 \geq m_2$). The mass-ratio q and total mass M are given by $q = m_1/m_2$ and $M = m_1 + m_2$, respectively. This paper is organized as follows. Section II describes the properties of the NR catalog used in this study, and succinctly describes signal-processing tools required for this analysis. Section III sheds light on the regions of parameter space that maximize the contribution of higher-order modes. In Section IV we quantify the importance of including higher-order waveform multipoles for GW detection in terms of signal-to-noise ratio (SNR) calculations. We show that Deep Filtering [3, 4] can identify these complex waveform signals in synthetic, simulated LIGO noise and real LIGO noise in Section V. We summarize our findings and future directions of work in Section VI.

II. NUMERICAL RELATIVITY CATALOG AND SIGNAL-PROCESSING TOOLS

We use a catalog of NR waveforms that we produced with the open source, NR software, the **Einstein Toolkit** [47–58] using the Blue Waters supercomputer. These simulations describe BBH mergers with mass-ratios $1 \leq q \leq 10$, and eccentricities $e_0 \leq 0.2$ ten cycles before merger. We extracted the modes $(\ell, |m|) = \{(2, 2), (2, 1), (3, 3), (3, 2), (3, 1), (4, 4), (4, 3), (4, 2), (4, 1)\}$ using the open source, software stack **POWER** [59]. Each NR waveform was produced with three different levels of resolution to quantify convergence. The detailed description of these analyses is presented in an accompanying article [60]. Table I summarizes the properties of these NR waveforms. We construct the waveform strain $h(t, \theta, \phi)$ using spin weight -2 spherical harmonics [61]

$$h(t, \theta, \phi) = h_+ - ih_\times = \sum_{\ell \geq 2} \sum_{-\ell \leq m \leq \ell} h^{\ell m}_{-2} Y_{\ell m}(\theta, \phi), \quad (1)$$

where (θ, ϕ) are spherical angles that define the direction of propagation. We define the waveform amplitude as $\mathcal{A} = \sqrt{h h^*}$, where h^* is the complex conjugate of the waveform strain h . Furthermore, the optimal matched-filter signal-to-noise ratio (SNR) is given by

$$H = F_+ h_+(\theta, \phi) + F_\times h_\times(\theta, \phi), \quad (2)$$

$$\text{SNR}^2 = 4\Re \int_{f_0}^{f_{\max}} \frac{\tilde{H} \tilde{H}^*}{S_n(f)} df, \quad (3)$$

TABLE I. Catalog of **Einstein Toolkit** numerical relativity waveforms. q is the mass-ratio, (e_0, ℓ_0, x_0) represent the measured values of eccentricity, mean anomaly, and dimensionless frequency parameters of the simulations.

Simulation	q	e_0	ℓ_0	x_0
E0001	1	0.060	3.50	0.077
J0045	2	0.078	3.35	0.079
J0061	4	0.065	2.90	0.086
L0016	5	0.195	3.20	0.084
P0001	6	0.057	2.50	0.0901
P0016	6	0.175	3.05	0.086
P0006	8	0.082	3.10	0.092
P0008	8	0.160	3.05	0.089
P0017	8	0.073	2.93	0.093
P0020	8	0.185	2.90	0.094
P0009	10	0.067	3.00	0.094
P0024	10	0.183	3.00	0.095

where $f_0 = 10\text{Hz}$ and $f_{\max} = 8192\text{Hz}$. \tilde{H} represents the Fourier transform of H ; (F_+, F_\times) are the antenna pattern response functions which depend on the sky position (α, β) of gravitational wave sources and the polarization angle ψ [62]. In this study, $S_n(f)$ is the one-sided noise power spectral density (PSD) corresponding to LIGO’s Zero Detuned High Power configuration [63].

III. HIGHER-ORDER WAVEFORM MULTIPOLES

GWs include the complete symphony of higher-order waveform modes. In this Section, we want to get insights about the regions of parameter space where their inclusion is critical for GW detection. To quantify the importance of including $(\ell, |m|)$ modes, we have carried out two complementary studies. The first one is motivated by the observation that higher-order modes become significant near merger [27]. To determine the (θ, ϕ) regions of parameter space that maximizes the contribution of $(\ell, |m|)$ modes near merger, we computed $[\mathcal{A}(\ell, |m|) - \mathcal{A}(\ell = 2, |m| = 2)](\theta, \phi)$. This quantity represents, at every (θ, ϕ) point, the amplitude peak difference between a waveform that includes all $(\ell, |m|)$ modes, and one that includes the $(\ell = 2, |m| = 2)$ only¹. Normalizing this quantity by the global maximum of $[\mathcal{A}(\ell = 2, |m| = 2)](\theta, \phi)$, i.e., $\mathcal{A}^{\max}(\ell = 2, |m| = 2)$, leads to

$$\Delta\mathcal{A} = \frac{[\mathcal{A}(\ell, |m|) - \mathcal{A}(\ell = 2, |m| = 2)](\theta, \phi)}{\mathcal{A}^{\max}(\ell = 2, |m| = 2)}. \quad (4)$$

Upon constraining this region of parameter space, we performed a complementary study to determine the (θ, ϕ)

¹ Hereafter the expression “all $(\ell, |m|)$ modes” refers to including the following modes $(\ell, |m|) = \{(2, 2), (2, 1), (3, 3), (3, 2), (3, 1), (4, 4), (4, 3), (4, 2), (4, 1)\}$.

parameter space where the inclusion of $(\ell, |m|)$ modes leads to a significant increase in the waveform amplitude, as compared to $(\ell, |m|) = (2, 2)$ waveforms, *throughout* the entire length of the NR waveforms. Inspired by

$$\Delta\mathcal{B} = \frac{[\mathcal{B}(\ell, |m|) - \mathcal{B}(\ell = 2, |m| = 2)](\theta, \phi)}{\mathcal{B}^{\max}(\ell = 2, |m| = 2)}, \quad (5)$$

$$\mathcal{B} = \int_{t=0}^T \mathcal{A}(t) dt, \quad (6)$$

where T represents the maximum time sample of a given NR waveform and, as mentioned above, $\mathcal{A} = \sqrt{h} \dot{h}^*$. As we describe below, using this metric enabled us to find the (θ, ϕ) regions of parameter space where the inclusion of higher-order modes leads to a significant SNR increase compared to waveforms that only include the $(\ell = 2, |m| = 2)$ mode.

Using the Mollweide projection $(\vartheta, \varphi) \rightarrow (\pi/2 - \theta, \phi - \pi)$, we present results of these combined analyses in the top two rows of Figure 1. Highlights of these results include

- The contribution of $(\ell, |m|)$ modes to the waveform strain changes significantly from case to case. Therefore, we have used different color bar ranges to emphasize the emergence of angular structure.
- The maxima of $\Delta\mathcal{A}(\vartheta, \varphi)$ correspond to the bright yellow regions. We have found that for all mass-ratios and eccentricities, the $(\ell = 2, |m| = 2)$ mode is maximized at $(\theta, \phi) = (0, 0)$, i.e., at the north pole in the Mollweide projection—a similar result is found in the context of quasi-circular BBHs. Elsewhere, the inclusion of $(\ell, |m|)$ modes boosts the waveform amplitude.
- The maxima of $\Delta\mathcal{B}$ are indicated by red diamonds. It is noteworthy that the maxima of $\Delta\mathcal{B}$ and $\Delta\mathcal{A}$ differ. This is an important finding that highlights the complex interplay between the topology of the spin-weight -2 spherical harmonics and the higher-order modes, which have a strong dependence on mass-ratio and eccentricity. In a nutshell, these results show that the (θ, ϕ) regions of parameter space that maximize the contribution of $(\ell, |m|)$ for GW detection are not equivalent to the (θ, ϕ) combinations that maximize the waveform amplitude near merger. We have confirmed this finding by computing the SNR distribution of signals that are constructed using the (θ, ϕ) combinations of the $\Delta\mathcal{A}$ peaks contained in the bright yellow regions of these maps, and waveforms constructed using the (θ, ϕ) combinations that correspond to the maxima of $\Delta\mathcal{B}$, or equivalently, the red diamonds in these

the time-domain SNR calculation procedure described in Section VI of [64] (see Eq. (64)), we computed the quantity

maps. Our SNR calculations indicate that the second class of waveforms lead to SNR values that are, on average, a factor of ~ 3 larger than the former class.

To obtain a visual representation of the importance of including higher-order modes for the detection of eccentric BBH mergers, the third and fourth rows of Figure 1 present a direct comparison between waveforms that include all $(\ell, |m|)$ modes and their $(\ell, |m|) = (2, 2)$ counterparts. These waveforms were constructed using the (ϑ, φ) combinations that represent the red diamonds in the top two rows of Figure 1. We observe that for eccentric BBH systems with mass-ratio $q \geq 5$, the inclusion of $(\ell, |m|)$ modes has a significant impact throughout the entire waveform evolution, with distinct signatures in the vicinity of merger which correspond to the imprint of higher-order waveform modes.

These results show that higher-order modes not only enhance the overall waveform amplitude, but also include noticeable modifications to the ringdown phase, in particular for asymmetric mass-ratio BBHs—see the insets in the panels of the third and fourth rows of Figure 1. Therefore, including $(\ell, |m|)$ is relevant both to enhance the detectability in new (θ, ϕ) regions of parameter space where $(\ell, |m|) = (2, 2)$ waveforms would otherwise be suppressed, and to accurately describe the merger evolution of eccentric BBH merger signals. These findings also imply that future tests of general relativity that aim to extract information from ringdown waveforms *must* include higher-order waveform modes to substantiate their claims, either in favor or against the correctness of general relativity to infer the nature of GW sources. In the following section we present a quantitative analysis of the importance of including higher-order waveform modes in terms of SNR calculations.

IV. SIGNAL-TO-NOISE RATIO CALCULATIONS

Having explored the (θ, ϕ) regions of parameter space that maximize the contribution of higher-order waveform multipoles, in this Section we compute the optimal matched-filter SNR distributions for a variety of eccentric BBHs. Since we are using a discrete set of NR waveforms, and these scale trivially with mass, we have considered BBHs with total mass $M = 60M_{\odot}$. This value is informed by GW observations of BBH mergers [8–12]. Furthermore, this astrophysically motivated choice implies that the merger phase of these BBHs will take place

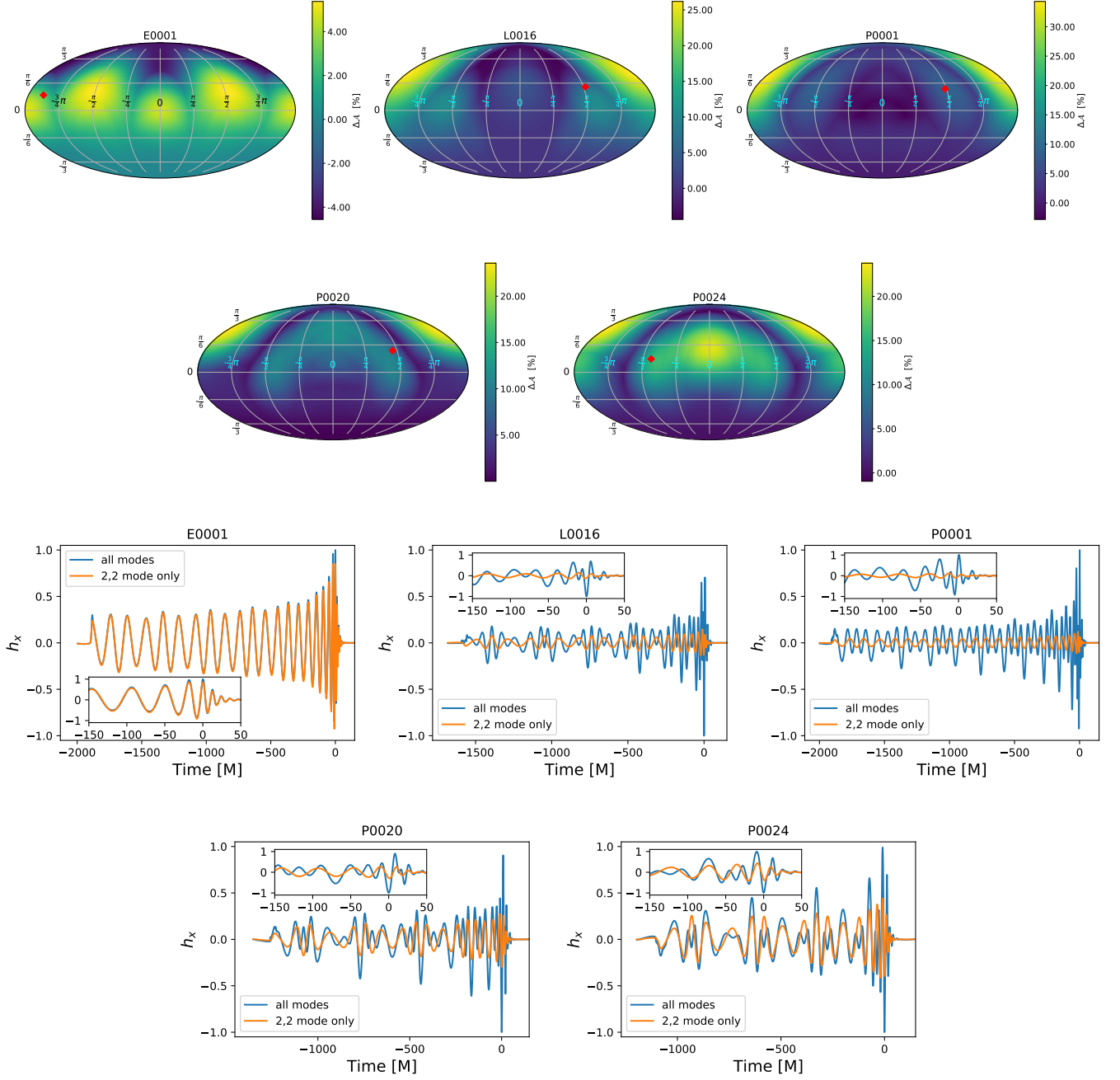


FIG. 1. First and second rows: The maps show the point-to-point amplitude peak difference, $\Delta\mathcal{A}$ in Eq. 4, between a waveform that includes $(\ell, |m|) = \{(2, 2) (2, 1), (3, 3), (3, 2), (3, 1), (4, 4), (4, 3), (4, 2), (4, 1)\}$ modes and one that only includes the $(\ell, |m|) = (2, 2)$ mode, normalized with respect to the global $(\ell, |m|) = (2, 2)$ amplitude maximum—see Eq. 4. The red diamonds, which correspond to the maxima of $\Delta\mathcal{B}$ in Eq. (5), indicate points where the inclusion of $(\ell, |m|)$ modes leads to a significant increase in the waveform amplitude, as compared to $(\ell, |m|) = (2, 2)$ waveforms, *throughout* the entire length of the waveform signals—see Eq. (5). These (θ, ϕ) maps were constructed using the Mollweide projection: $(\vartheta, \varphi) \rightarrow (\pi/2 - \theta, \phi - \pi)$. Third and fourth rows: Comparison between waveforms that include either all $(\ell, |m|)$ modes or the $(\ell, |m|) = (2, 2)$ mode only, using (ϑ, φ) values that correspond to the location of the red diamonds in the top panels.

in LIGO's optimal sensitivity frequency range, thereby maximizing the contribution of higher-order waveform multipoles to the SNR of these systems.

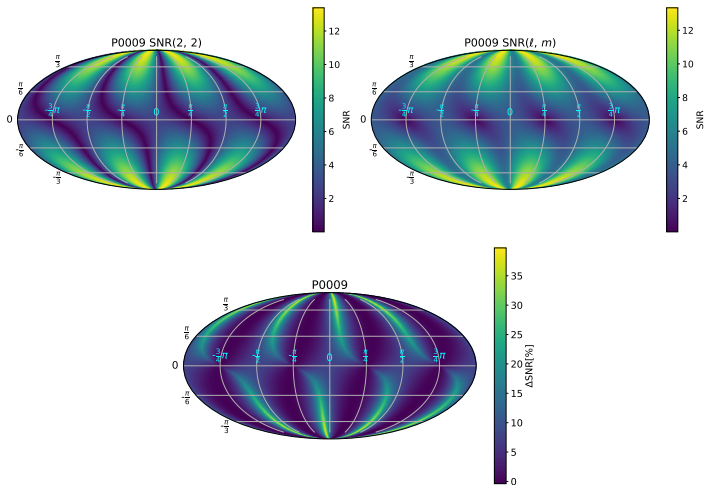


FIG. 2. Top panels, from left to right: SNR distributions produced either by $(\ell = 2, |m| = 2)$ or $(\ell, |m|)$ NR waveforms, respectively. Bottom panel: metric used to quantify the importance of including higher-order waveform multipoles, given by Eq. (7). The effect of including $(\ell, |m|)$ modes is to enhance the detectability in sky regions (α, β) where $(\ell = 2, |m| = 2)$ NR waveforms are significantly suppressed. In these calculations, the total mass of the BBH is $60M_\odot$, the distance to the source is 500Mpc and the polarization angle $\psi = \pi/4$.

The goal of this section is to quantify the potential SNR increase due to the inclusion of higher-order waveform modes. To do so, we use Eq. (1) for two cases, namely, when all the $(\ell, |m|)$ modes are included and when only the $(\ell = 2, |m| = 2)$ is considered, and use (θ^*, ϕ^*) values that maximize the inclusion of $(\ell, |m|)$ modes for SNR calculations—represented by red diamonds in the top panels of Figure 1. Using these waveforms, we compute their corresponding SNRs at each sky location (α, β) , i.e., $\text{SNR}^{(2,2)} \rightarrow \text{SNR}(\ell = 2, |m| = 2; \theta^*, \phi^*; \alpha, \beta)$ and $\text{SNR}^{(\ell,m)} \rightarrow \text{SNR}(\ell, |m|; \theta^*, \phi^*; \alpha, \beta)$. Finally, we subtract these quantities and normalize them using the global $\text{SNR}^{(2,2)}$ maximum, i.e.,

$$\Delta\text{SNR} = \frac{\text{SNR}^{(\ell,m)} - \text{SNR}^{(2,2)}}{\text{SNR}_{\text{max}}^{(2,2)}}. \quad (7)$$

Figure 2 demonstrates the use of this metric to quantify the effect of including higher-order waveform multipoles. As shown in these panels, the main effect of including $(\ell, |m|)$ modes is to enable the detectability of GWs in (α, β) sky regions where waveforms that only include the $(\ell = 2, |m| = 2)$ mode are significantly suppressed, and thereby poorly recovered or entirely missed. Using Eq. (7), and setting $\psi = \pi/4$, we present a set of SNR distributions in Figure 3 for a variety of eccentric BBH systems. These results indicate that

- E0001. Higher-order waveform multipoles can be safely ignored for equal mass BBHs.
- L0016. The inclusion of higher-order waveform modes has a significant impact in the detectability of $q = 5$ eccentric BBH mergers, boosting the SNR in new (α, β) regions by up to $\sim 30\%$.
- P0001. For $q = 6$ eccentric BBH mergers, the SNR is enhanced by up to $\sim 35\%$ with respect to waveforms that only include the $(\ell = 2, |m| = 2)$ mode.
- P0020. Including higher-order modes for $q = 8$ eccentric BBH mergers can boost the SNR in new (α, β) regions up to $\sim 40\%$.
- P0024. $q = 10$ eccentric BBH mergers report the largest SNR increase, reaching values up to $\sim 45\%$ in new (α, β) regions.

In summary, observing eccentric BBH mergers with SNR gains up to $\gtrsim 45\%$ in sky locations where $(\ell = 2, |m| = 2)$ mode waveforms would otherwise be suppressed provides enough incentive to develop GW searches that include higher-order modes. This approach will be critical to search for and find these astrophysically motivated compact binary sources.

Having shed light on the quantitative aspect of including $(\ell, |m|)$ modes for GW detection, the second aspect of this study involves the development of an algorithm to extract GWs that include higher-order waveform multipoles. In the following section we show that the deep learning algorithms we pioneered for gravitational wave astrophysics [3, 4] in the context of waveforms that only include the $(\ell, |m|) = (2, 2)$ mode can also be used to identify GW signals that include $(\ell, |m|)$ modes. This is the first demonstration in the literature that deep learning can extract higher-order waveform multipole signals from eccentric BBH mergers both in simulated and real LIGO noise.

V. DETECTION OF ECCENTRIC BINARY BLACK HOLE MERGERS WITH DEEP LEARNING ALGORITHMS

The first demonstration that machine learning can detect and characterize GWs in simulated LIGO noise was introduced in [3]. This work established that deep learning is as sensitive as a matched-filtering based search, orders of magnitude more computationally efficient, and capable of detecting eccentric and spin-precessing GW signals that only include the $(\ell = 2, |m| = 2)$ mode. The extension of that analysis to a realistic detection scenario using raw advanced LIGO noise was introduced for the first time in [4]. In this section, we show that these algorithms can also be utilized to detect and characterize GWs whose morphology is significantly more complex than the datasets used to train our neural networks, i.e., non-spinning and quasi-circular BBH systems.

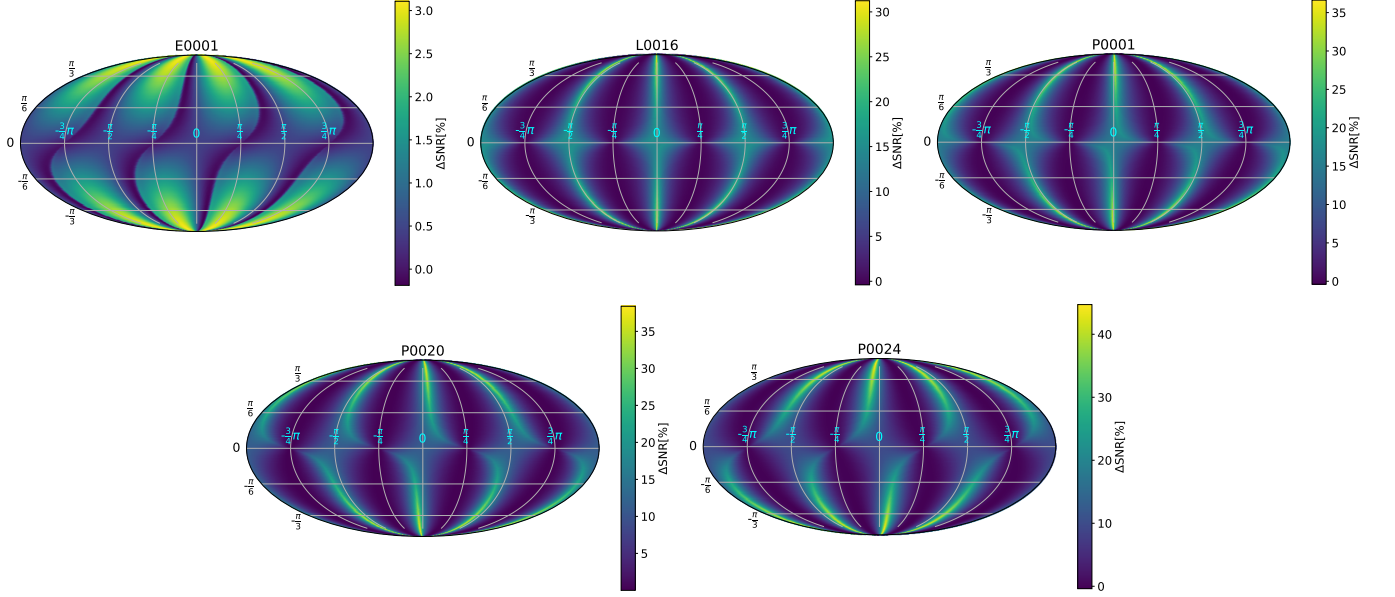


FIG. 3. Point-to-point SNR difference between waveforms that include all $(\ell, |m|)$ modes and waveforms that only include the $(\ell, |m|) = (2, 2)$ mode, normalized with respect to the $(\ell = 2, |m| = 2)$ global SNR maximum—see Eq. 7. The waveforms are constructed using the (θ, ϕ) combinations that maximize the contribution of waveform modes in either case, indicated by red diamonds in the top panels of Figure 1. The SNR distributions are presented as a function of the source’s sky location (α, β) mapped into a Mollweide projection: $(\vartheta, \varphi) \rightarrow (\pi/2 - \alpha, \beta - \pi)$. We have set the polarization angle $\psi = \pi/4$ in these calculations.

A detailed description of the construction of our neural networks can be found in [3, 4]. To quantify the sensitivity with which deep learning can extract eccentric, higher-order waveform multipole signals, we selected from our catalog of NR waveforms those that have the most complex topology. Thereafter, we embedded these NR waveforms in simulated LIGO noise, and quantified the optimal matched-filter SNR at which these signals may be detected with our deep learning algorithms. The results of this analysis, assuming simulated noise from LIGO’s Zero Detuned High Power configuration [63], are presented in Figure 4. We notice that independently of the (q, e) of the systems, we achieve 100% sensitivity for all these BBH systems when $\text{SNR} \geq 10$ with a false alarm rate that we tuned to be 1%, i.e., 1 per 100 seconds of noise in our test dataset was misclassified as signals. It is remarkable that this result is the same in the context of quasi-circular BBH signals that we reported in [3].

We have extended this analysis using real LIGO noise that we obtained from the LIGO Open Science Center. To carry out this analysis, we used the neural network model described in [4]. To assess the power of this algorithm to identify an entirely new class of GW signals in a realistic detection scenario, we injected the most complex eccentric NR signals we produced in our datasets in real LIGO noise corresponding to GW150914. In Figure 4, we show that Deep Filtering can detect GWs signals that include higher-order waveform modes with the same sensitivity it can detect GWs used to train the neural network model, i.e., non-spinning, quasi-circular BBH

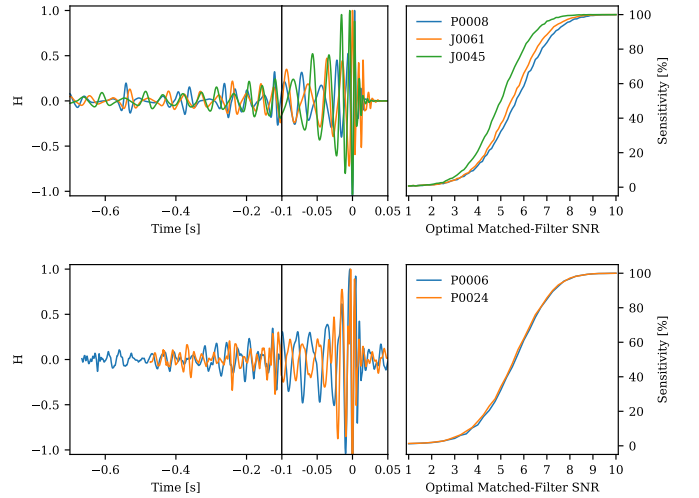


FIG. 4. Top left panel: $H(t)$, see Eq. (2), whitened with simulated LIGO noise for three NR waveforms with $M = 80M_\odot$ and $(\theta^*, \phi^*, \alpha, \beta, \psi)$ combinations that maximize the contribution of $(\ell, |m|)$ modes. Top right panel: **Deep Filtering** reaches 100% Sensitivity to identify all these signals in simulated Gaussian noise for optimal matched-filter $\text{SNR} \geq 10$. Bottom left panel: as above but now using real LIGO noise to whiten two NR waveforms that represent highly asymmetric mass-ratio, eccentric BBH signals. Bottom right panel: **Deep Filtering** attains 100% Sensitivity when these signals have optimal matched-filter $\text{SNR} \geq 10$.

mergers [4].

These results can be further improved by using multiple detectors and enforcing coincidence, reducing the false alarm rate to (0.01%, 0.0001%) for 2- and 3-detector networks, respectively. We can further decrease this false alarm rate value by using a variety of methods, such as changing the fraction of noise used during the training stage, ensuring that the estimated parameters of the source from each detector are consistent, and by running consistency checks with matched-filtering pipelines that use a reduced template bank whose modeled waveforms are close to our predicted parameters.

This work further exhibits the power and resilience of neural networks to generalize to new types of signals and enable the identification of an entirely new class of GW sources. It must be emphasized that, at present, there is no matched-filtering algorithm to extract eccentric GW signals from simulated or real LIGO data. Therefore, this analysis represents the first successful attempt at correctly identifying a new class of GW signals both in simulated and real LIGO noise datasets.

We have also found that Deep Filtering can measure the total mass of the signals with an accuracy $\leq 15\%$ both using simulated and real LIGO noise. Given these encouraging results, in the near future we will present an improved version of these deep learning algorithms that are adequate to *detect* and *characterize* eccentric binary mergers in real LIGO data, providing information about the masses and spins of the binary components, and the orbital eccentricity.

VI. CONCLUSION

We have quantified the impact of higher-order waveform multipoles for the detection of non-spinning black holes on eccentric orbits in terms of SNR calculations. We have found that while they become significant for asymmetric BBH systems, it is also the case that these results depend heavily on three important ingredients: the angular structure of the spin-weight -2 spherical harmonics, and the mass-ratio and eccentricity of the system. In view of these findings, it is essential to develop models that include higher-order waveform multipoles for actual GW searches of eccentric BBH mergers.

We have also demonstrated for the first time that machine learning can effectively extract these complex GW signals from simulated and real LIGO noise with the same sensitivity it identifies quasi-circular GW signals. Even though the deep learning algorithm we used for this analysis was only trained with non-spinning BHs on quasi-circular orbits, it was robust enough to generalize to an entirely new class of signals, whose morphology is significantly more complex than their quasi-circular counterparts. In future work, we will present a new class of neural network algorithms for the detection and characterization of spinning black holes on eccentric orbits.

VII. ACKNOWLEDGEMENTS

This research is part of the Blue Waters sustained-petascale computing project, which is supported by the National Science Foundation (awards OCI-0725070 and ACI-1238993) and the State of Illinois. Blue Waters is a joint effort of the University of Illinois at Urbana-Champaign and its National Center for Supercomputing Applications. The eccentric numerical relativity simulations used in this article were generated with the open source, community software, the Einstein Toolkit on the Blue Waters petascale supercomputer. We acknowledge support from NVIDIA, Wolfram Research, the NCSA and the SPIN (Students Pushing INnovation) Program at NCSA. NSF-1550514 and NSF-1659702 grants are gratefully acknowledged. We thank the **NCSA Gravity Group** for useful feedback and suggestions.

Appendix A: Interplay of mass-ratio and eccentricity for gravitational wave detection

The top panels of Figure 5 present the (θ, ϕ) regions of parameter space where the $(\ell, |m|)$ modes contribute significantly to GW detection. The two selected cases can be directly compared to the results presented in the second row of Figure 1. We note that even though (P0017, P0020) and (P0024, P0009) have the same mass-ratio, their different eccentricities lead to significantly different (θ, ϕ) angular distributions. The bottom panels of Figure 5 correspond to their respective SNR distributions, produced using the same approach described in Section IV. The results presented in Figures 1 and 5 exhibit the strong dependence of higher-order modes both on mass-ratio and eccentricity. The bottom panels of Figure 5 presents sky maps for the SNR distributions of P0017 and P0009 using $\psi = 0$.

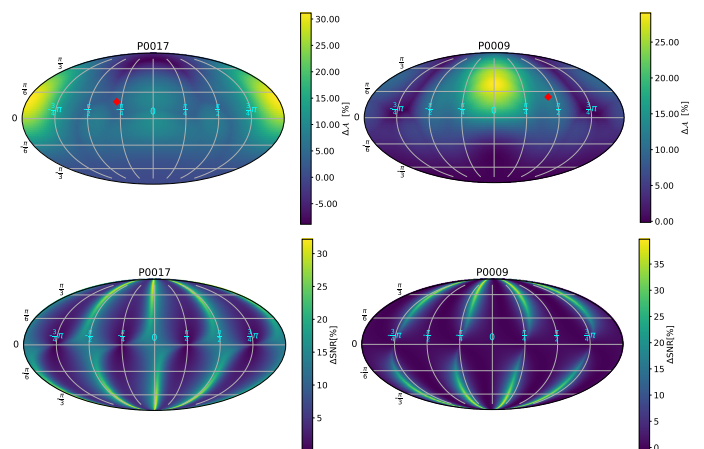


FIG. 5. Compare the pairs (P0017, P0020) and (P0009, P0024). P0020 and P0024 are presented in the second row of Figure 1.

-
- [1] J. Strader, L. Chomiuk, T. J. Maccarone, J. C. A. Miller-Jones, and A. C. Seth, *Nature (London)* **490**, 71 (2012), [arXiv:1210.0901 \[astro-ph.HE\]](#).
- [2] C. J. Hailey *et al.*, *Nature* **556** (2018), 10.1038/nature25029.
- [3] D. George and E. A. Huerta, *Phys. Rev. D* **97**, 044039 (2018), [arXiv:1701.00008 \[astro-ph.IM\]](#).
- [4] D. George and E. A. Huerta, *Physics Letters B* **778**, 64 (2018), [arXiv:1711.03121 \[gr-qc\]](#).
- [5] B. P. Abbott, R. Abbott, T. D. Abbott, M. R. Abernathy, F. Acernese, K. Ackley, C. Adams, T. Adams, P. Addesso, R. X. Adhikari, and *et al.*, *Physical Review Letters* **116**, 131103 (2016), [arXiv:1602.03838 \[gr-qc\]](#).
- [6] The LIGO Scientific Collaboration, J. Aasi, *et al.*, *Classical and Quantum Gravity* **32**, 074001 (2015), [arXiv:1411.4547 \[gr-qc\]](#).
- [7] F. Acernese *et al.*, *Classical and Quantum Gravity* **32**, 024001 (2015), [arXiv:1408.3978 \[gr-qc\]](#).
- [8] B. P. Abbott, R. Abbott, T. D. Abbott, M. R. Abernathy, F. Acernese, K. Ackley, C. Adams, T. Adams, P. Addesso, R. X. Adhikari, and *et al.*, *Physical Review Letters* **116**, 061102 (2016), [arXiv:1602.03837 \[gr-qc\]](#).
- [9] B. P. Abbott, R. Abbott, T. D. Abbott, M. R. Abernathy, F. Acernese, K. Ackley, C. Adams, T. Adams, P. Addesso, R. X. Adhikari, and *et al.*, *Physical Review Letters* **116**, 241103 (2016), [arXiv:1606.04855 \[gr-qc\]](#).
- [10] B. P. Abbott, R. Abbott, T. D. Abbott, M. R. Abernathy, F. Acernese, K. Ackley, C. Adams, T. Adams, P. Addesso, R. X. Adhikari, *et al.*, *Physical Review Letters* **118**, 221101 (2017).
- [11] B. P. Abbott, R. Abbott, T. D. Abbott, F. Acernese, K. Ackley, C. Adams, T. Adams, P. Addesso, R. X. Adhikari, V. B. Adya, and *et al.*, *Physical Review Letters* **119**, 141101 (2017), [arXiv:1709.09660 \[gr-qc\]](#).
- [12] B. P. Abbott, R. Abbott, T. D. Abbott, F. Acernese, K. Ackley, C. Adams, T. Adams, P. Addesso, R. X. Adhikari, V. B. Adya, and *et al.*, *Astrophys. J. Lett* **851**, L35 (2017), [arXiv:1711.05578 \[astro-ph.HE\]](#).
- [13] B. P. Abbott, R. Abbott, T. D. Abbott, F. Acernese, K. Ackley, C. Adams, T. Adams, P. Addesso, R. X. Adhikari, V. B. Adya, and *et al.*, *Physical Review Letters* **119**, 161101 (2017), [arXiv:1710.05832 \[gr-qc\]](#).
- [14] B. P. Abbott, R. Abbott, T. D. Abbott, F. Acernese, K. Ackley, C. Adams, T. Adams, P. Addesso, R. X. Adhikari, V. B. Adya, and *et al.*, *Astrophys. J. Lett* **848**, L12 (2017), [arXiv:1710.05833 \[astro-ph.HE\]](#).
- [15] D. A. Coulter, R. J. Foley, C. D. Kilpatrick, M. R. Drout, A. L. Piro, B. J. Shappee, M. R. Siebert, J. D. Simon, N. Ulloa, D. Kasen, B. F. Madore, A. Murguía-Berthier, Y.-C. Pan, J. X. Prochaska, E. Ramirez-Ruiz, A. Rest, and C. Rojas-Bravo, *Science* **358**, 1556 (2017), [arXiv:1710.05452 \[astro-ph.HE\]](#).
- [16] F. Antonini and H. B. Perets, *Astrophys. J.* **757**, 27 (2012).
- [17] F. Antonini, N. Murray, and S. Mikkola, *Astrophys. J.* **781**, 45 (2014), [arXiv:1308.3674 \[astro-ph.HE\]](#).
- [18] F. Antonini, *Astrophys. J.* **794**, 106 (2014), [arXiv:1402.4865](#).
- [19] F. Antonini, S. Chatterjee, C. L. Rodriguez, M. Morscher, B. Pattabiraman, V. Kalogera, and F. A. Rasio, *Astrophys. J.* **816**, 65 (2016), [arXiv:1509.05080](#).
- [20] J. Samsing and E. Ramirez-Ruiz, *Astrophys. J. Lett* **840**, L14 (2017), [arXiv:1703.09703 \[astro-ph.HE\]](#).
- [21] J. Samsing, M. MacLeod, and E. Ramirez-Ruiz, *Astrophys. J.* **784**, 71 (2014), [arXiv:1308.2964 \[astro-ph.HE\]](#).
- [22] J. Samsing, *ArXiv e-prints* (2017), [arXiv:1711.07452 \[astro-ph.HE\]](#).
- [23] J. Samsing, A. Askar, and M. Giersz, *Astrophys. J.* **855**, 124 (2018), [arXiv:1712.06186 \[astro-ph.HE\]](#).
- [24] J. Samsing, D. J. D’Orazio, A. Askar, and M. Giersz, *ArXiv e-prints* (2018), [arXiv:1802.08654 \[astro-ph.HE\]](#).
- [25] C. L. Rodriguez, P. Amaro-Seoane, S. Chatterjee, and F. A. Rasio, *Physical Review Letters* **120**, 151101 (2018), [arXiv:1712.04937 \[astro-ph.HE\]](#).
- [26] E. A. Huerta, P. Kumar, B. Agarwal, D. George, H.-Y. Schive, H. P. Pfeiffer, R. Haas, W. Ren, T. Chu, M. Boyle, D. A. Hemberger, L. E. Kidder, M. A. Scheel, and B. Szilagyi, *Phys. Rev. D* **95**, 024038 (2017), [arXiv:1609.05933 \[gr-qc\]](#).
- [27] E. A. Huerta, C. J. Moore, P. Kumar, D. George, A. J. K. Chua, R. Haas, E. Wessel, D. Johnson, D. Glennon, A. Rebei, A. M. Holgado, J. R. Gair, and H. P. Pfeiffer, *Phys. Rev. D* **97**, 024031 (2018), [arXiv:1711.06276 \[gr-qc\]](#).
- [28] P. C. Peters, *Phys. Rev.* **136**, B1224 (1964).
- [29] P. C. Peters and J. Mathews, *Phys. Rev. D* **131**, 435 (1963).
- [30] D. Clausen, S. Sigurdsson, and D. F. Chernoff, *MNRAS* **428**, 3618 (2013), [arXiv:1210.8153 \[astro-ph.HE\]](#).
- [31] I. Hinder, L. E. Kidder, and H. P. Pfeiffer, *ArXiv e-prints* (2017), [arXiv:1709.02007 \[gr-qc\]](#).
- [32] K. Cannon, R. Cariou, A. Chapman, M. Crispin-Ortuzar, N. Fotopoulos, M. Frei, C. Hanna, E. Kara, D. Keppel, L. Liao, S. Privitera, A. Searle, L. Singer, and A. Weinstein, *Astrophys. J.* **748**, 136 (2012), [arXiv:1107.2665 \[astro-ph.IM\]](#).
- [33] S. A. Usman *et al.*, *Classical and Quantum Gravity* **33**, 215004 (2016), [arXiv:1508.02357 \[gr-qc\]](#).
- [34] H. Shen, D. George, E. A. Huerta, and Z. Zhao, *ArXiv e-prints* (2017), [arXiv:1711.09919 \[gr-qc\]](#).
- [35] Z. Cao and W.-B. Han, *ArXiv e-prints* (2017), [arXiv:1708.00166 \[gr-qc\]](#).
- [36] T. Hinderer and S. Babak, *ArXiv e-prints* (2017), [arXiv:1707.08426 \[gr-qc\]](#).
- [37] J. Levin, S. T. McWilliams, and H. Contreras, *Classical and Quantum Gravity* **28**, 175001 (2011), [arXiv:1009.2533 \[gr-qc\]](#).
- [38] N. Yunes, K. G. Arun, E. Berti, and C. M. Will, *Phys. Rev. D* **80**, 084001 (2009), [arXiv:0906.0313 \[gr-qc\]](#).
- [39] E. A. Huerta, P. Kumar, S. T. McWilliams, R. O’Shaughnessy, and N. Yunes, *Phys. Rev. D* **90**, 084016 (2014), [arXiv:1408.3406 \[gr-qc\]](#).
- [40] E. A. Huerta and D. A. Brown, *Phys. Rev. D* **87**, 127501 (2013), [arXiv:1301.1895 \[gr-qc\]](#).
- [41] I. Hinder, F. Herrmann, P. Laguna, and D. Shoemaker, *Phys. Rev. D* **82**, 024033 (2010).
- [42] N. Loutrel and N. Yunes, *Classical and Quantum Gravity* **34**, 044003 (2017), [arXiv:1607.05409 \[gr-qc\]](#).
- [43] N. Loutrel, N. Yunes, and F. Pretorius, *Phys. Rev. D* **90**, 104010 (2014), [arXiv:1404.0092 \[gr-qc\]](#).
- [44] T. Osburn, N. Warburton, and C. R. Evans, *Phys. Rev. D* **93**, 064024 (2016), [arXiv:1511.01498 \[gr-qc\]](#).

- [45] N. Loutrel and N. Yunes, *Classical and Quantum Gravity* **34**, 135011 (2017), [arXiv:1702.01818 \[gr-qc\]](#).
- [46] B. Moore, T. Robson, N. Loutrel, and N. Yunes, *ArXiv e-prints* (2018), [arXiv:1807.07163 \[gr-qc\]](#).
- [47] T. Nakamura, K. Oohara, and Y. Kojima, *Progress of Theoretical Physics Supplement* **90**, 1 (1987).
- [48] M. Shibata and T. Nakamura, *Phys. Rev. D* **52**, 5428 (1995).
- [49] T. W. Baumgarte and S. L. Shapiro, *Phys. Rev. D* **59**, 024007 (1998), [gr-qc/9810065](#).
- [50] J. G. Baker, J. Centrella, D.-I. Choi, M. Koppitz, and J. van Meter, *Physical Review Letters* **96**, 111102 (2006), [gr-qc/0511103](#).
- [51] M. Campanelli, C. O. Lousto, P. Marronetti, and Y. Zlochower, *Physical Review Letters* **96**, 111101 (2006), [gr-qc/0511048](#).
- [52] D. Pollney, C. Reisswig, E. Schnetter, N. Dorband, and P. Diener, *Phys. Rev. D* **83**, 044045 (2011), [arXiv:0910.3803 \[gr-qc\]](#).
- [53] B. Wardell, I. Hinder, and E. Bentivegna, “Simulation of GW150914 binary black hole merger using the Einstein Toolkit,” (2016).
- [54] F. Löffler, J. Faber, E. Bentivegna, T. Bode, P. Diener, R. Haas, I. Hinder, B. C. Mundim, C. D. Ott, E. Schnetter, G. Allen, M. Campanelli, and P. Laguna, *Classical and Quantum Gravity* **29**, 115001 (2012), [arXiv:1111.3344 \[gr-qc\]](#).
- [55] M. Ansorg, B. Brügmann, and W. Tichy, *Phys. Rev. D* **70**, 064011 (2004), [arXiv:gr-qc/0404056](#).
- [56] P. Diener, E. N. Dorband, E. Schnetter, and M. Tiglio, *J. Sci. Comput.* **32**, 109 (2007), [arXiv:gr-qc/0512001](#).
- [57] E. Schnetter, S. H. Hawley, and I. Hawke, *Class. Quantum Grav.* **21**, 1465 (2004), [arXiv:gr-qc/0310042](#).
- [58] J. Thornburg, *Class. Quantum Grav.* **21**, 743 (2004), [arXiv:gr-qc/0306056](#).
- [59] D. Johnson, E. A. Huerta, and R. Haas, *Classical and Quantum Gravity* **35**, 027002 (2018), [arXiv:1708.02941 \[gr-qc\]](#).
- [60] E. A. Huerta *et al.*, (2018).
- [61] L. Blanchet, *Living Reviews in Relativity* **9**, 4 (2006).
- [62] L. S. Finn, *Phys. Rev. D* **63**, 102001 (2001), [gr-qc/0010033](#).
- [63] D. Shoemaker, “Advanced LIGO anticipated sensitivity curves,” (2015), <https://dcc.ligo.org/LIGO-T0900288-v2/public>.
- [64] L. Barack and C. Cutler, *Phys. Rev. D* **69**, 082005 (2004), [arXiv:gr-qc/0310125](#).